

Electronic Supplementary Information

3D Tree-shaped Hierarchical Flax Fabric for Highly Efficient Solar Steam Generation

Yaping Li^{a,b}, *Jie Fan*^{a,b*}, *Run Wang*^b, *Wan Shou*^c, *Liang Wang*^b, *Yong Liu*^{b*}

a. Key Laboratory of Advanced Textile Materials (Tiangong University), Ministry of Education, Tianjin, 300387, China

b. School of Textile Science and Engineering, Tiangong University, Tianjin, 300387, China

c. Department of Mechanical and Aerospace Engineering, Missouri University of Science and Technology, Rolla, MO, USA

* Corresponding author Email; fanjie@tiangong.edu.cn (Dr. J. Fan), liuyong@tiangong.edu.cn (Dr. Y. Liu)

S1. Weave structure design of TBFF

Flax yarns were purchased from commercial market. Plied yarn was prepared using a twisting machine (DSTw-01, Tianjin Jiacheng, China). Then, twist added on the plied flax yarns were set in pressure vessel under 115°C, 100% humidity, and 1.7 atmospheric pressure for 1h. Then, it was fully dried at ambient condition. Finally, the TBFF was carried out using a semi-automatic

weaving prototype (Tianjin Jiacheng, China). In the TBFF, the warp yarns move back and forth between the two surface layers of the fabric (see Fig. S1), providing continuous water transport paths from PWL, BWL to FL.

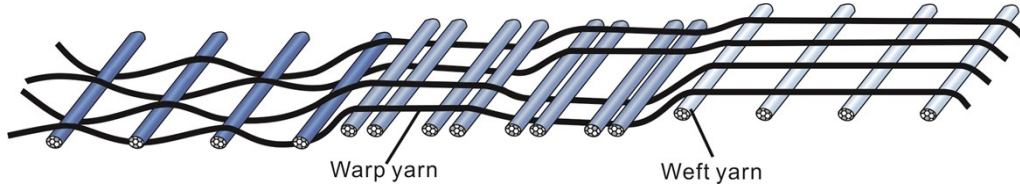


Fig. S1. Interweaving structure of three groups of warp and weft yarns with different layers in different layers in the TBFF.

S2. Continuous water transport paths of TBFF-PDA-PPy

The dynamic water transport spread along the continuous water transport paths of warp yarns (the blue warp yarn in Fig. S2a) in the TBFF. To illustrate the water transport paths, we had conducted the experiments in Fig. S2b. The rhodamine B aqueous solutions as a tracer dye for detecting the water distribution was dropped into FL of TBFF. Then, the water was rapidly diffused along the continuous water transport paths of warp yarns according to the cross-sectional fluorescence images of the TBFF-PDA-PPy. Because the TBFF-PDA-PPy has no interlaced structure in the thickness direction of TBFF-PDA-PPy (from PWL to FL) in circulating weave unit of FL, which hinders water transport in vertical direction. Besides, even though through water penetration by contact between PWL, BWL and FL, the water is hardly transported in vertical direction, because the contact area is quite small between warp yarns and four weft yarns in the FL. Finally, the continuous water transport paths of warp yarns were preferentially selected to transport water in the TBFF-PDA-PPy. the dynamic water transport spread along the continuous water transport paths of warp yarns in the TBFF-PDA-PPy. This is inconsistent with the transpiration of the tree.

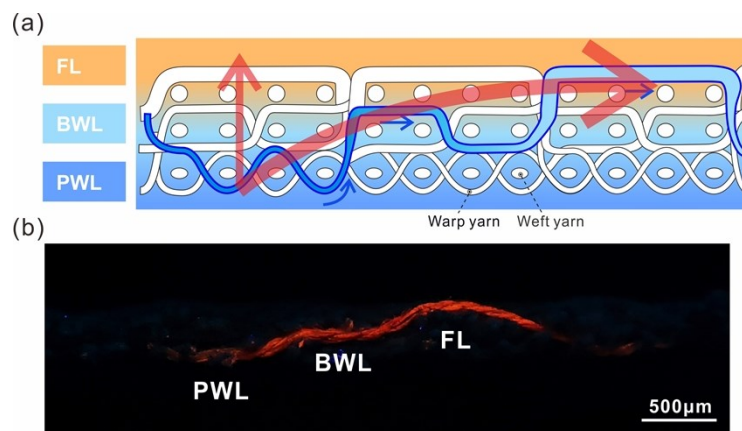


Fig. S2. (a) Schematic illustration of water transport paths from PWL, BWL to FL via the discontinuous vertical path and the continuous long water transport path of warp yarns in the TBFF-PDA-PPy. (b) Fluorescence images of the cross-section of the TBFF-PDA-PPy after a droplet of rhodamine B was dropped on the fabric surface (observed in ultra-violet (365nm) lamp box), suggesting that the longer water transport path along the continuous warp yarn is more efficient for water transportation.

S3. Weave structure design of SFF

The SFF was designed as the control sample. The cross section of SFF is shown in Fig. S3. The warp and weft yarns of SFF with three layers forms stitch structure between the adjacent two layers. As a result, there is discontinuous yarns moving back and forth between the two surfaces of the SFF.

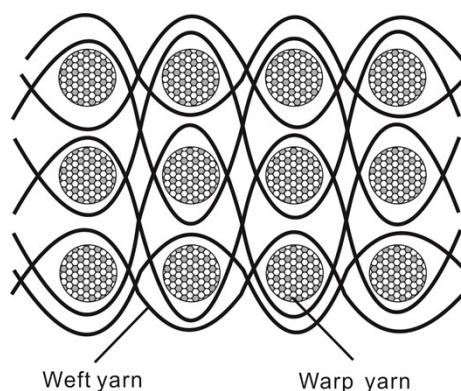


Fig. S3. The schematic diagram of SFF.

S4. Weave structure parameters of TBFF and SFF

The detailed structural parameters TBFF and SFF were shown in the Table S1.

Table S1. The weave structure parameters TBFF and SFF.

Samples	Metric count	Grams per square meter (g/m ²)	Thickness (mm)	Twist (twist/10 cm)	Reed number	Warp density (yarns/10 cm)	Weft density (yarns/10 cm)
TBFF	15	1035	3.225	38	60	377	160
SFF	15	1030	2.425	38	60	377	160

S5. Setup of the solar-driven water evaporation experiment

The solar-driven water evaporation system is present in Fig. S4a, b. The MF located between the photo-thermal layer (TBFF-PDA-PPy) and the bulk water has a 3D web structure and good hydrophilicity (Fig. S2c), which can pump water upward and efficiently control the water supply to the fabric.

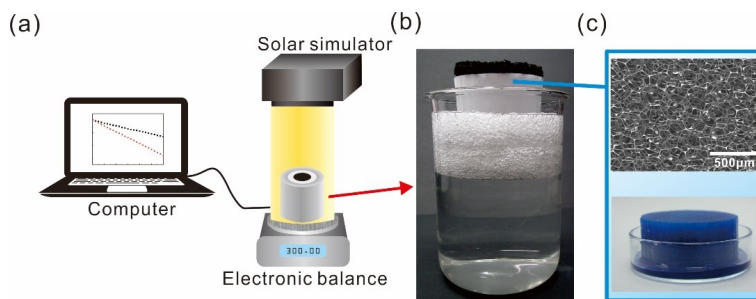


Fig. S4. (a) Simplified diagram of solar steam generating devices. (b) Photographs of TBFF-PDA-PPy placing on top surface of MF and PS foam and floating on the pure water. (c) The SEM of MF and photographs of MF to uptake water (stained with methylene blue) in steady-state situation.

S6. Weave structure of SFF-PDA-PPy

The SFF was designed as the control sample, which has the same surface morphology on both sides and was changed the color to black in Fig. S5a, b. The warp and weft yarns of SFF with three layers forms stitch between the adjacent two layers in Fig. S5c. As a result, there are discontinuous yarns moving back and forth between the two surfaces of the SFF.

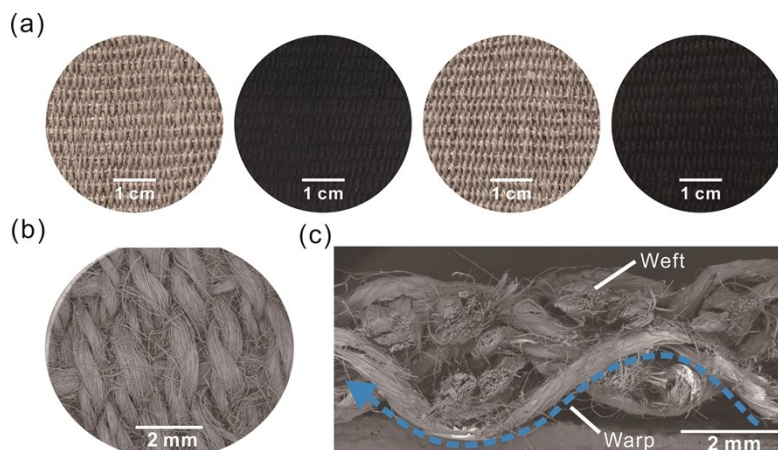


Fig. S5. (a) Optical images of SFF and SFF-PDA-PPy in one side and SFF-PDA-PPy in the other side. (b) SEM of SFF. (c) Cross section of SFF (Inset: blue curve represents discontinuous water channel for both side of SFF).

S7. Water management of SFF-PDA-PPy

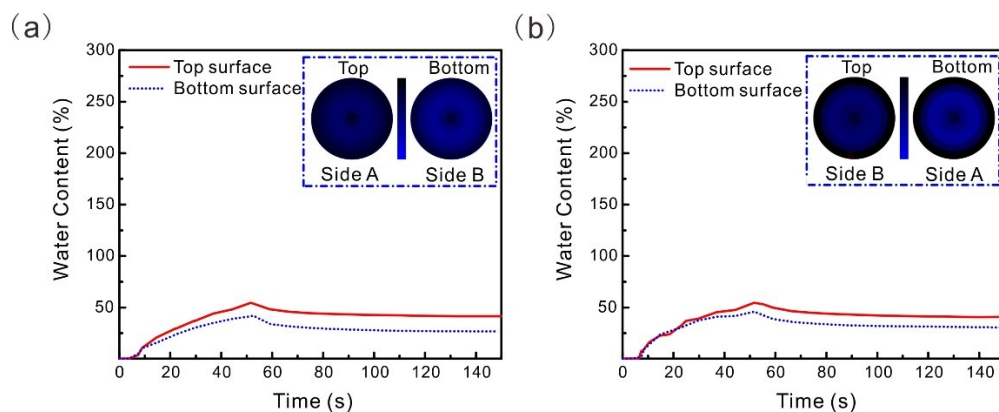


Fig. S6. MMT of SFF-PDA-PPy with one side A facing up (a) and the other side B facing up (b).

S8. Investigation of light absorption

The reflectance and transparency of the TBFF samples were measured by a UV-vis-NIR spectrophotometer, as displayed in Fig. S7a, b. Compared to original TBFF, TBFF-PDA-PPy

had a poor reflectance ($\approx 0.2\%$) and transmittance ($\approx 0\%$) in the whole wide wavelength range and maintained a stable performance during the reuse process.

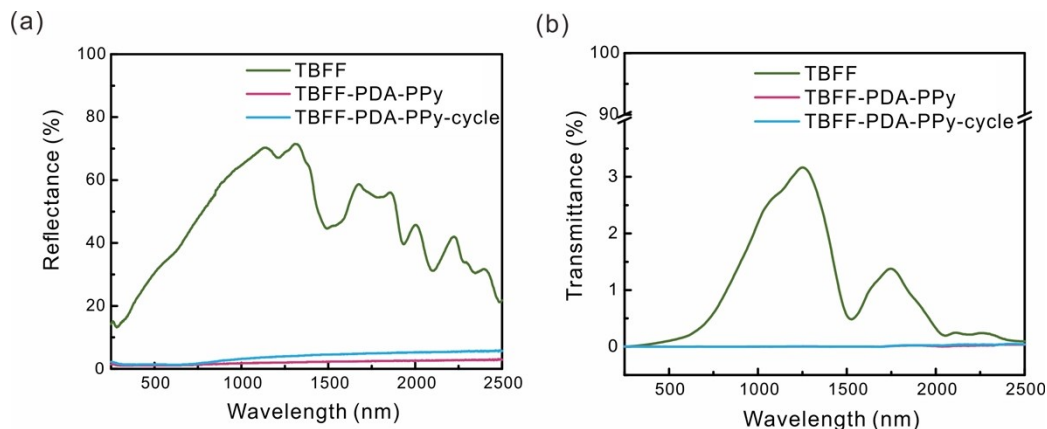


Fig. S7. (a) Reflectance spectra of the TBFF-PDA-PPy. (b) Transmittance spectra of the TBFF-PDA-PPy.

S9. Infrared thermal imaging of TBFF-PDA-PPy

Photograph of dry TBFF-PDA-PPy is shown in Fig. S8a. The infrared thermal image of dry TBFF-PDA-PPy shows that the fabric surface temperature can quickly rise to $75.5\text{ }^{\circ}\text{C}$ in 10 mins under 1 sun irradiation and remains stable in Fig. S8b.

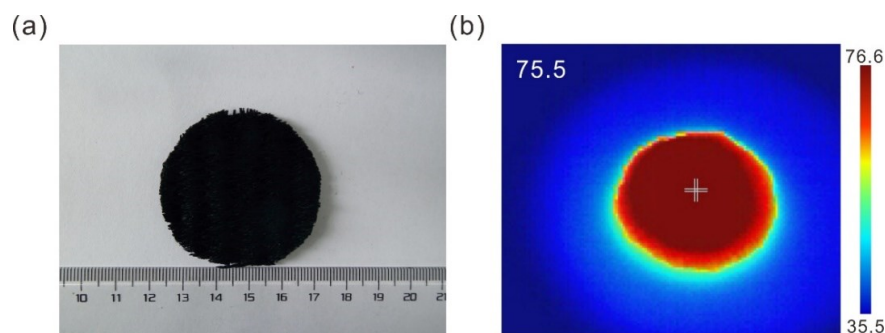


Fig. S8. (a) The photograph of TBFF-PDA-PPy. (b) Infrared thermal image of TBFF-PDA-PPy under 1 sun for 10 min.

S10. Stability of TBFF-PDA-PPy-F

To confirm the stable performance of TBFF-PDA-PPy-F for long-time use, the solar steam generation experiments were repeated 10 times under 1 kW m^{-2} illumination. The result is shown that the evaporation rates remained essentially unchanged in Fig. S9a, indicating the excellent stability of TBFF-PDA-PPy. Meanwhile, it can be seen the surface morphology of the TBFF-PDA-PPy-F in Fig. S9b, the fibrous morphology of PPy-PDA coating on the surface of the fiber didn't peel off from the fabric or degrade during solar steam generation after 10 cycles under 1 sun, demonstrating the mechanical stability of the PPy-PDA coating on the surface of the TBFF.

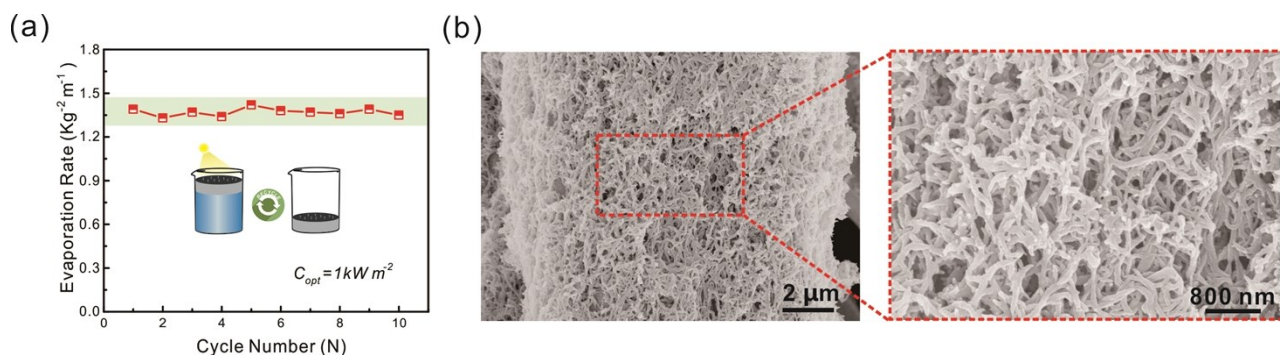


Fig. S9. (a) Evaporation rate of the TBFF-PDA-PPy-F for 10 cycles under 1 sun. (b) SEM images of surface morphology of the TBFF-PDA-PPy-F after 10 cycles under 1 sun.

S11. Wicking performance and evaporation performance of single-layer fabric

To illustrate the advantage from TBFF-PDA-PPy-F evaporation system in terms of evaporation performance, single-layer plain weave flax fabric modified by PDA-PPy (S-PWFF-PDA-PPy) and basket weave flax fabric (S-BWFF-PDA-PPy) with the same construction parameters were prepared as that of the corresponding layer of the TBFF-PDA-PPy-F. It should be noted that the FL can't separately constitute a single layer fabric, because there is not interlacing between the warp yarn and weft yarn. The surface and cross section morphologies of the S-PWFF-PDA-PPy and S-BWFF-PDA-PPy are shown in Fig. S10a-b, indicating S-PWFF-PDA-PPy and S-BWFF-PDA-PPy has no hierarchical structure.

Water wicking performance of the S-PWFF-PDA-PPy and S-BWFF-PDA-PPy were carried out with the rhodamine B as a tracer dye in the aqueous solutions. When the wicking test started, the bottom of black strips ($1 \text{ cm} \times 12 \text{ cm}$) of S-PWFF-PDA-PPy and S-BWFF-PDA-PPy were

quickly dipped into the rhodamine B aqueous solutions. After a certain time, the strips of the two fabrics were taken out of the liquid and put into the ultra-violet (365nm) lamp box to observe the wicking height of the liquid. The fluorescence images of the S-PWFF-PDA-PPy and S-BWFF-PDA-PPy and the corresponding wicking height-time curves of the two fabrics are shown in Fig. S10c, d. The result suggests that the S-BWFF-PDA-PPy shows faster wicking velocity and higher final wicking height comparing with the S-PWFF-PDA-PPy, because the S-BWFF-PDA-PPy has more continuous liquid transport paths in the yarns owing to low frequent interlacing between the warp yarns and weft yarns.

The evaporation performance of S-PWFF-PDA-PPy and S-BWFF-PDA-PPy were investigated. As shown in Fig. S10e, the UV-vis-NIR absorption spectra of the S-PWFF-PDA-PPy and S-BWFF-PDA-PPy suggest that the light absorption of S-PWFF-PDA-PPy and S-BWFF-PDA-PPy is 96% and 94% respectively in a wide wavelength range from 240 to 2,500 nm, which were lower than that of TBFF-PDA-PPy (98%). When the S-PWFF-PDA-PPy and S-BPWFF-PDA-PPy were placed on the solar-driven water evaporation system, the surface temperature of S-PWFF-PDA-PPy and S-BWFF-PDA-PPy were recorded. As shown in Fig. S10f, the S-PWFF-PDA-PPy has a higher surface temperature than S-BWFF-PDA-PPy. The time-dependent water mass change curves of the S-PWFF-PDA-PPy and S-BWFF-PDA-PPy under 1 sun are shown in Fig. S10g. The S-PWFF-PDA-PPy shows a lower evaporation rate ($1.15 \text{ kg m}^{-2} \text{ h}^{-1}$) than that of the S-BWFF-PDA-PPy ($1.18 \text{ kg m}^{-2} \text{ h}^{-1}$). Correspondingly, the solar thermal conversion efficiency of S-PWFF-PDA-PPy and S-BWFF-PDA-PPy were 73.3% and 75.4%, respectively, which is lower than that of the TBFF-PDA-PPy (87.4%). Therefore, the different weave structures of the S-PWFF-PDA-PPy and S-BWFF-PDA-PPy plays an important role in wicking performance and the solar thermal conversion efficiency. Thus, the design of the TBFF-PDA-PPy with a 3D hierarchical structure was demonstrated to be a superior photo-thermal material for SSG.

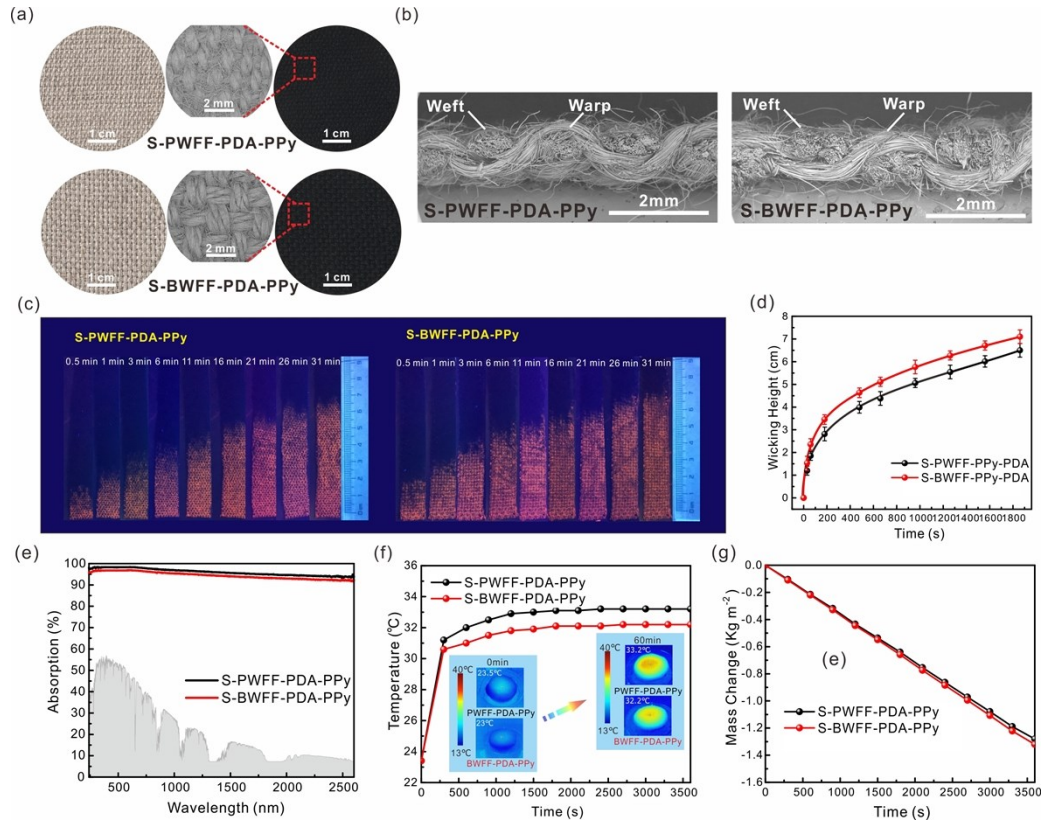


Fig. S10 (a) Optical images and SEM of S-PWFF, S-BWFF, S-PWFF-PDA-PPy, and S-BWFF-PDA-PPy. (b) SEM images of the cross-section of the S-PWFF-PDA-PPy and S-BWFF-PDA-PPy. (c) Fluorescence images of the wicking height for S-PWFF-PDA-PPy and S-BWFF-PDA-PPy in different time (using rhodamine B as tracer dye in the aqueous solutions, observed in ultra-violet (365nm) lamp box). (d) Wicking height-time curves of the S-PWFF-PDA-PPy and BWFF-PDA-PPy. (e) UV-vis-NIR absorption spectra of the S-PWFF-PDA-PPy and S-BWFF-PDA-PPy. The gray area represents normalized spectral solar irradiance (AM 1.5 G). (f) Time-dependent temperature curves and infrared images of S-PWFF-PDA-PPy and S-BWFF-PDA-PPy under 1 sun. (g) Mass change of S-PWFF-PDA-PPy and S-BWFF-PDA-PPy under 1 sun.

S12. Energy loss analysis for the fabric evaporator

The energy loss in TBFF-PDA-PPy under input heat flux of 1 kW m^{-2} (q_i) is divided into five parts: (1) water evaporation, (2) reflection energy loss on the surface of the fabric, (3) conductive heat loss to bulk water, (4) radiation heat loss from the fabric to the environment, and (5) convection heat loss from the fabric to the environment. The detailed calculation of energy loss is illustrated below.

(1) Water evaporation

The water evaporation consumption rate is equal to the steady-state evaporation efficiency, i. e. η_{eva} is 87.4%.

(2) Reflection energy loss

The reflection energy loss is equal to the reflectance of the TBFF-PDA-PPy ($\eta_{ref} \approx 2.1\%$).

(3) Conductive heat loss

The conductive heat loss is calculated based on Fourier's law, which is calculated as follows:

$$Q_{cond} = k \frac{\Delta T}{L} \quad (S1)$$

where k is the thermal conductivity of the wet MF ($0.31 \text{ W m}^{-1} \text{ K}^{-1}$) and $\Delta T/L$ is the gradient of temperature for permeating the bulk water. The temperature gradient is approximately 130 K/m

as measured by IR image. Therefore, $\eta_{cond} = \frac{Q_{cond}}{q_{in}} = \frac{k\Delta t/L}{q_{in}} = \frac{0.31 \times 130}{1000} \approx 4.03\%$

(4) Radiation heat loss

Radiation heat loss can be calculated using the Stefan-Boltzmann law:

$$Q_{rad} = \varepsilon \sigma (T_2^4 - T_1^4) \quad (S3)$$

where ε denotes emissivity of TBFF-PDA-PPy-F (0.91), σ denotes the Stefan-Boltzmann constant, which is $5.67 \times 10^{-8} \text{ W m}^{-2} \text{ K}^{-4}$. T_2 is the top surface temperature of TBFF-PDA-PPy-F system (32.4°C), T_1 (27°C) is the adjacent environment temperature. Thus,

$$\eta_{rad} = \frac{Q_{rad}}{q_{in}} = \frac{\varepsilon \sigma (T_2^4 - T_1^4)}{q_{in}} \approx \frac{0.91 \times 5.67 \times 10^{-8} (305.4^4 - 300^4)}{1000} \approx 3.09\%$$

(5) convection heat loss

The heat convection loss per unit area can be calculated by Newton's law of cooling.

$$Q_{conv} = h(T_2 - T_1) \quad (S4)$$

where h is the convection heat transfer coefficient, which is approximately $5 \text{ W m}^{-2} \text{ K}^{-1}$,

$$\eta_{conv} = \frac{Q_{conv}}{q_{in}} = \frac{h(T_2 - T_1)}{q_{in}} \approx \frac{5 \times (305.4 - 300)}{1000} \approx 2.7\%$$

Therefore,

In summary, the total energy is about 99.32 % of q_i (i.e. 87.4 % + 2.1% + 4.03 % + 3.09 % + 2.7 % \approx 99.32 %), which approximately obey the energy conservation law while a small part of the remaining energy may be caused by the estimation uncertainties or the measuring instrument.

S13. Comparison of solar steam generation performance of reported photo-thermal materials

Table S2. Advantages of TBFF-PDA-PPy compared the solar steam generation performance of reported photo-thermal materials modified by PPy or PDA and based on fabric as a substrate under 1 sun irradiation (1 kW m^{-2}).

Materials	Characteristic	Efficiency (%)	Ref.
TBFF-PDA-PPy-F	Low cost, high evaporation, easy-preparation, excellent adhesive force	87.4	This work
PEGylated MoS ₂ coat cotton cloth	High cost	80.5	1
Ag nanoparticles modified floating carbon cloth	High cost	92.39	2
Multi-walled carbon nanotube loading on cotton fabric	Low efficiency	86.01	3
Carbon fabric	Low efficiency	60.2	4
Black polyester plain fabric	Low efficiency	48.3	5
Cellulose-based fabric	Low efficiency	57 ± 2.5	6
Activated carbon fiber	Low efficiency	79.4	7
Cotton fabric deposited candle soot	Poor adhesive force	86.3	8
2D-dyed towel-foam and 3D-dyed towel-foam	Poor stability of organic dyes	86.2/96.8	9
Reduced graphene oxide-silk-fabric	High cost	102	10
Polyaniline coating cotton fabric	Complex process	89.9	11
3D PPy-modified cotton	Low efficiency	~80	12
PPy coated cotton fabric	Low efficiency	82.4	13

Monolithic PPy sponge	Low efficiency	84.72	14
Kapok fibers-PPy aerogels.	Low efficiency/high cost	82.4	15
PPy coated stainless steel mesh	Low efficiency/high cost	58	16
PPy-wood	Low efficiency	83	17
Bacterial nanocellulose loading with PDA	Low efficiency	78	18
PDA coated carbonized cotton	Complex process	88	19
TiO ₂ -PDA/PPy/cotton	High cost/complex process	98	20

Table S3. Comparison of the solar steam generation performances of some natural and low-cost photo-thermal materials under 1 sun irradiation (1 kW m⁻²).

Category	Substrate material	Fabrication of photo-thermal materials	3D Hierarchical structure	Mechanical properties	Mass production	Evaporation rate [kg m ⁻² h ⁻¹]	Efficiency [%]	Ref.
Fabric	Flax fabric	One-step synthesis (PPy-PDA)	Yes	Excellent	Yes	1.37	87.4	This work
	Activated carbon fiber felt	Commercially obtainable	No	Excellent	Yes	1.22	79.4	7
	Cellulose fabric	Commercially obtainable	No	Excellent	Yes	-	~57	6
	Cotton fabric	One-step synthesis (PPy)	No	Excellent	Yes	1.2	82.4	13
	Cotton fabric	Multi-step synthesis (PANI)	No	Excellent	Yes	1.94	>89.9	11
	Cotton fabric	Thermal deposition (candle soot)	No	Excellent	No	1.375	86.3	8
	Black polyester fabric	Spinning (CB)	No	Excellent	Yes	0.57	48.3	5
	Blank hollow spacer fabric	Multi-step synthesis (Chitosan-rGO)	No	Excellent	Yes	1.4352	86	21
	Carbon fabric	Hydrothermal synthesis (TiO ₂ nanorods)	No	Excellent	Yes	0.9	60.2	4
	Carbon cloth	Multi-step synthesis (Ag NPs)	No	Excellent	Yes	1.36	92.39	2
Natural plant	Wood	Carbonization	Yes	Excellent	No	<1	57.3	22

	Mushrooms	Carbonization	Yes	Poor	No	1.475	78	23
	Lotus leaf	Carbonization	Yes	Poor	No	1.33	90	24
	Sunflower heads	Carbonization	Yes	Poor	No	1.51	100.4	25
	Eggshell	Carbonization	No	Poor	No	1.31	78	26
Paper	Facial tissue	Carbonization	No	Poor	No	<1	64	27
	White paper	Ultrasonic deposition (CB)	No	Poor	Yes	1.28	88	28
	Filter paper	Spray-coating (GO)	Yes	Poor	Yes	-	85	29
	Airlaid paper	Multi-step synthesis (AuNPs)	No	Poor	Yes	-	77.8	30
	Cellulose paper	One-step synthesis (PPy)	No	Poor	Yes	2.99	85.9	31

Notes: Polyaniline (PANI), carbon black (CB), reduced graphene oxide (rGO), nanoparticles (NPs), graphene oxide (GO).

S14. Water content states of SFF-PDA-PPy

In this solar-driven water evaporation experiment, the efficient water supply is according to capillary action to pumping of water towards the heating region. And the water distributes in the micro capillaries between fibers on the top yarns of surface, which is major evaporation region. The solar-driven water evaporation experiment managed to avoid excessive water (gravity water) presenting and locating between yarns. Because the macro pores with gravity water for vapor evaporation are completely blocked and meanwhile the larger volume water accumulation decreases the solar steam efficiency due to large heat loss.

The surface water content of SFF-PDA-PPy was captured by digital microscope in Fig. S11. In comparison, the warp yarns of SFF-PDA-PPy is more extrusion and bending than that of TBFF-PDA-PPy-F but less than that of TBFF-PDA-PPy-P. Besides, the SFF-PDA-PPy provides larger macro slim space than TBFF-PDA-PPy-F between the warp yarns lead to smaller vapor evaporation area. Owing to discontinuous micro water transfer paths, the capillary water of SFF-PDA-PPy supply less than TBFF-PDA-PPy-F and TBFF-PDA-PPy-P. Therefore, the SFF-PDA-PPy exhibits lower efficiency than TBFF-PDA-PPy-F.

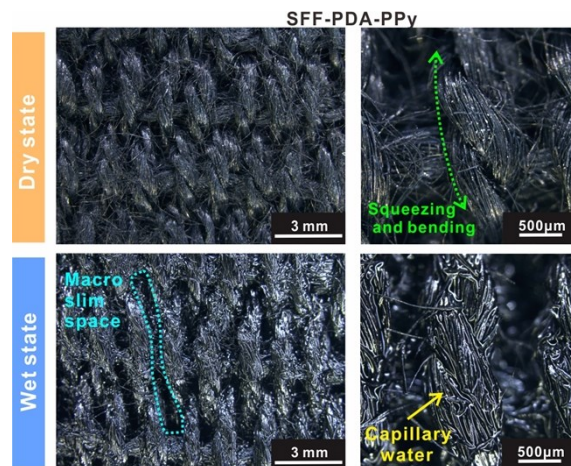


Fig. S11. The optical images of SFF-PDA-PPy with relatively less interlacing and squeezing between the warp yarns and the weft yarns in dry state and water content on the surface of SFF-PDA-PPy with more macro slim lead to less evaporation area in wet working state.

S15. The solar desalination device for collecting purified water.



Fig. S12. Photograph of the solar desalination device for collecting purified water. Vapor condenses on the wall of glass and water flows to the bottom.

REFERENCES

1. Z. Guo, G. Wang, X. Ming, T. Mei, J. Wang, J. Li, J. Qian and X. Wang, *ACS Appl. Mater. Interfaces*, 2018, **10**, 24583-24589.

2. P. Qiao, J. Wu, H. Li, Y. Xu, L. Ren, K. Lin and W. Zhou, *ACS Appl. Mater. Interfaces*, 2019, **11**, 7066-7073.
3. Q. Qi, Y. Wang, W. Wang, X. Ding and D. Yu, *Sci. Total Environ.*, 2020, **698**, 134136.
4. M. W. Higgins, A. R. Shakeel Rahmaan, R. R. Devarapalli, M. V. Shelke and N. Jha, *Sol. Energy*, 2018, **159**, 800-810.
5. J. He, T. R. Foysal, H. Yang, M. Islam, L. Li, W. Li and W. Cui, *Mater. Lett.*, 2020, **261**, 126962.
6. G. Ni, S. H. Zandavi, S. M. Javid, S. V. Boriskina, T. A. Cooper and G. Chen, *Energy Environ. Sci.*, 2018, **11**, 1510-1519.
7. H. Li, Y. He, Y. Hu and X. Wang, *ACS Appl. Mater. Interfaces*, 2018, **10**, 9362-9368.
8. S. Gao, X. Dong, J. Huang, J. Dong, F. D. Maggio, S. Wang, F. Guo, T. Zhu, Z. Chen and Y. Lai, *Global Challenges*, 2019, **3**, 1800117.
9. Y. Yang, Y. Sui, Z. Cai and B. Xu, *Global Challenges*, 2019, **3**, 1900004.
10. Q. Zhang, X. Xiao, G. Wang, X. Ming, X. Liu, H. Wang, H. Yang, W. Xu and X. Wang, *J. Mater. Chem. A*, 2018, **6**, 17212-17219.
11. Z. Liu, B. Wu, B. Zhu, Z. Chen, M. Zhu and X. Liu, *Adv. Funct. Mater.*, 2019, **29**, 1905485.
12. P. Xiao, J. Gu, C. Zhang, F. Ni, Y. Liang, J. He, L. Zhang, J. Ouyang, S.-W. Kuo and T. Chen, *Nano Energy*, 2019, **65**, 104002.
13. D. Hao, Y. Yang, B. Xu and Z. Cai, *Appl. Therm. Eng.*, 2018, **141**, 406-412.
14. Y. Fan, W. Bai, P. Mu, Y. Su, Z. Zhu, H. Sun, W. Liang and A. Li, *Sol. Energy Mater. Sol. Cells*, 2020, **206**, 110347.
15. P. Mu, W. Bai, Y. Fan, Z. Zhang, H. Sun, Z. Zhu, W. Liang and A. Li, *J. Mater. Chem. A*, 2019, **7**, 9673-9679.
16. L. Zhang, B. Tang, J. Wu, R. Li and P. Wang, *Adv. Mater.*, 2015, **27**, 4889-4894.
17. W. Huang, G. Hu, C. Tian, X. Wang, J. Tu, Y. Cao and K. Zhang, *Sustain. Energy Fuels*, 2019, **3**, 3000-3008.
18. Q. Jiang, H. Gholami Derami, D. Ghim, S. Cao, Y.-S. Jun and S. Singamaneni, *J. Mater. Chem. A*, 2017, **5**, 18397-18402.
19. X. Wu, L. Wu, J. Tan, G. Y. Chen, G. Owens and H. Xu, *J. Mater. Chem. A*, 2018, **6**, 12267-12274.
20. D. Hao, Y. Yang, B. Xu and Z. Cai, *ACS Sustainable Chem. Eng.*, 2018, **6**, 10789-10797.
21. F. Wang, D. Wei, Y. Li, T. Chen, P. Mu, H. Sun, Z. Zhu, W. Liang and A. Li, *J. Mater. Chem. A*, 2019, **7**, 18311-18317.
22. M. Zhu, Y. Li, G. Chen, F. Jiang, Z. Yang, X. Luo, Y. Wang, S. D. Lacey, J. Dai, C. Wang, C. Jia, J. Wan, Y. Yao, A. Gong, B. Yang, Z. Yu, S. Das and L. Hu, *Adv. Mater.*, 2017, **29**, 1704107.
23. N. Xu, X. Hu, W. Xu, X. Li, L. Zhou, S. Zhu and J. Zhu, *Adv. Mater.*, 2017, **29**, 1606762.
24. Y. Tian, H. Yang, S. Wu, J. Yan, K. Cen, T. Luo, G. Xiong, Y. Hou, Z. Bo and K. Ostrikov, *Nano Energy*, 2019, **66**, 104125.
25. P. Sun, W. Zhang, I. Zada, Y. Zhang, J. Gu, Q. Liu, H. Su, D. Pantelić, B. Jelenković and D. Zhang, *ACS Appl. Mater. Interfaces*, 2020, **12**, 2171-2179.
26. X. Han, W. Wang, K. Zuo, L. Chen, L. Yuan, J. Liang, Q. Li, P. M. Ajayan, Y. Zhao and J. Lou, *Nano Energy*, 2019, **60**, 567-575.
27. Y. Chen, Y. Shi, H. Kou, D. Liu, Y. Huang, Z. Chen and B. Zhang, *ACS Sustainable Chem. Eng.*, 2019, **7**, 2911-2915.

28. Z. Liu, H. Song, D. Ji, C. Li, A. Cheney, Y. Liu, N. Zhang, X. Zeng, B. Chen, J. Gao, Y. Li, X. Liu, D. Aga, S. Jiang, Z. Yu and Q. Gan, *Global Challenges*, 2017, **1**, 1600003.
29. X. Li, R. Lin, G. Ni, N. Xu, X. Hu, B. Zhu, G. Lv, J. Li, S. Zhu and J. Zhu, *National Science Review*, 2017, **5**, 70-77.
30. Y. Liu, S. Yu, R. Feng, A. Bernard, Y. Liu, Y. Zhang, H. Duan, W. Shang, P. Tao, C. Song and T. Deng, *Adv. Mater.*, 2015, **27**, 2768-2774.
31. F. Ni, P. Xiao, C. Zhang, Y. Liang, J. Gu, L. Zhang and T. Chen, *ACS Appl. Mater. Interfaces*, 2019, **11**, 15498-15506.